Large Carrier Mobilities in ErMnO3 Conducting Domain Walls Revealed by Quantitative Hall Effect Measurements

Turner, P. W., McConville, J. P. V., McCartan, S. J., Campbell, M. H., Schaab, J., McQuaid, R. G. P., Kumar, A., & Gregg, J. M. (2018). Large Carrier Mobilities in ErMnO3 Conducting Domain Walls Revealed by Quantitative Hall Effect Measurements. *Nano Letters*, *18*(10), 6381-6386. https://doi.org/10.1021/acs.nanolett.8b02742

Published in:
Nano Letters

Document Version:
Peer reviewed version

Large Carrier Mobilities in $ErMnO_3$ Conducting Domain Walls Revealed by Quantitative Hall Effect Measurements

P. W. Turner[1], J. P. V. McConville[1], S. J. McCartan[1], M. H. Campbell[1], J. Schaab[2], R. G. P. McQuaid[1], A. Kumar[1], J. M. Gregg[1*]*

[1] *Centre for Nanostructured Media, School of Mathematics and Physics, Queen's University Belfast, University Road, BELFAST, N. Ireland, U. K. BT71NN.*

[2] *Department of Materials, ETH Zurich, Vladimir-Prelog-Weg 4, 8093 Zurich, Switzerland.*

*email: m.gregg@qub.ac.uk or pturner04@qub.ac.uk

KEYWORDS: Ferroelectric Domain walls, Conduction, Carrier mobilities, Hall microscopy

Abstract

Kelvin Probe Force Microscopy (KPFM) has been used to directly and quantitatively measure Hall voltages, developed at conducting tail-to-tail domain walls in $ErMnO_3$ single crystals, when current is driven in the presence of an approximately perpendicular magnetic field. Measurements across a number of walls, using two different atomic force microscope platforms, consistently suggest that the active p-type carriers have unusually large room temperature mobilities: of the

order of hundreds of square centimetres per volt second ($cm^2V^{-1}s^{-1}$); associated carrier densities were estimated to be of the order of $10^{13}cm^{-3}$. Such mobilities, at room temperature, are high in comparison to both bulk oxide conductors and $LaAlO_3$-$SrTiO_3$ sheet conductors. High carrier mobilities are encouraging for the future of domain-wall nanoelectronics and, significantly, also suggest the feasibility of meaningful investigations into dimensional confinement effects in these novel domain wall systems.

Almost 50 years ago, Hans Schmid and co-workers reported their suspicions that domain walls in oxyfluoride multiferroics could possess significantly enhanced conductivity compared to bulk[1]. Around the same time, Vul *et al.* [2] postulated that charged domain walls (with opposing polarization vectors) should be metallic: a prediction subsequently corroborated, to some extent, by Grekov *et al.*[3]. Some thirty years later, Aird and Salje[4] presented experimental evidence for domain wall superconductivity in reduced tungsten trioxide, and Mizuuchi *et a l*[5] discussed how domain wall conduction and associated undesirable effects on poling in MgO:$LiNbO_3$ might be obviated. Despite these reports, it was not until high-resolution direct current maps of bismuth ferrite films were published, in 2009 [6], that the prospect of harnessing domain walls as mobile conducting conduits, in new kinds of agile nanocircuitry, began to be taken seriously. Since then, the field of "domain wall nanoelectronics"[7] has emerged strongly; teams have discovered domain wall conduction in a number of systems: from the well-known proper ferroelectric materials, such as lead zirconate titanate[8], barium titanate[9], and lithium niobate[10,11], to slightly more obscure improper ferroelectrics, such as the rare-earth manganites[12], Ruddleson-Popper titanates[13] and copper-chlorine boracites[14]. Precise control over the injection and movement of ferroelectric domain walls has also been developed[15–17], taking the lead from strategies already honed in race-track nanomagnetics research and ferromagnetic domain wall logic[18,19]. Excitingly, in the last year, control over injection of conducting domain walls, between source and drain electrodes, has allowed land-mark demonstrator resistance memory

devices to be made[20,21]. In addition, very recently, domain wall-electrode junctions have been shown to facilitate alternating current rectification at the nanoscale[22].

Despite this impressive progress towards devices, comparatively little research has been done on the fundamental transport physics associated with conducting domain walls. One study, by Campbell *et al.*[23], has reported preliminary Hall effect measurements, taken specifically on tail-to-tail charged walls in $YbMnO_3$ single crystals. Although these measurements gave reasonable indications of carrier densities and mobilities, it is important to note that the quantification of the Hall voltage measured was indirect, relying entirely on calibration experiments to allow signals developed, in the topography channel of the scanning probe set-up used, to be interpreted in terms of absolute voltage levels. To give more rigorous quantitative information, direct mapping of the Hall voltage developed at conducting domain walls is needed; herein we report that this can be done, using Kelvin Probe Force Microscopy (KPFM), a scanning probe technique that allows true spatial mapping of surface potential. Implications of results obtained are consistent with the Campbell *et al.* study, insofar as they confirm that p-type carriers are active in conducting tail-to-tail charged walls in the hexagonal manganites; however, in the current report, significantly higher carrier mobilities are found. In fact, our quantitative Hall investigations suggest that carrier mobilities, in manganite domain walls, have room temperature values that are comparable to, or higher than, any seen in conducting oxide systems to date.

The hexagonal rare-earth manganites ($RMnO_3$, where R denotes the rare-earth ion [Dy, Ho, Er, Tm, Yb, Lu, Y, Sc]) show symmetry breaking from a high temperature $P6_3/mmc$ phase, to a low temperature $P6_3cm$ phase [24–26]. The structural changes associated with this symmetry reduction involve tilting of Mn-centred oxygen polyhedra and c-axis oriented displacements of the rare-earth ions[27,28], creating three structural and two dipolar domain states (which combine to generate six distinct domain variants). The microstructures in these manganite systems are characterised by meandering domain walls which converge at six-fold junctions (sometimes referred to as “vortices”), illustrated by the in-plane piezoresponse force microscopy (PFM) images taken from the $ErMnO_3$ crystal, which was the subject of the present work (Figs 1a and b). In this case, ferroelectric polarisation was almost entirely in-plane, indicated by extremely low

out-of-plane PFM amplitude (not shown). While there is evidence that all domain walls in manganites can act as electrical conductors at high driving voltages[29], conventional conducting atomic force microscopy (cAFM) reveals the tendency for the most obvious conduction, under modest d.c. driving voltages, to occur at tail-to-tail charged walls (Figs 1c and d).

To perform Hall effect measurements, gold electrodes were sputtered onto polished thin $ErMnO_3$ crystal surfaces, such that a network of conducting domain walls straddled the interelectrode gap (Fig 2a). An external d.c. power supply was used to drive current along the conducting walls, while a magnetic field was applied parallel to the sample surface and perpendicular to the electric field (and also approximately parallel / antiparallel to the polarisation directions in the system). Carriers migrating along the conducting domain walls, under the externally applied d.c. bias, experience a Lorentz force and aggregate at, or are denuded from, the line of intersection between the domain wall and the sample surface (the surface trace of the domain wall). This results in a local change in the surface potential which can be monitored, in principle, using KPFM (Fig 2b and c). KPFM is a scanning probe technique which involves an initial line scan, using conventional tapping mode atomic force microscopy (AFM), to establish the local surface topography. Subsequently, the same line is retraced at a constant lift height above the topography (typically of the order of tens of nanometres) and the d.c. bias at the tip, needed to negate the influence of local electrostatic forces experienced at that lift-height, is monitored. This d.c. tip bias is an absolute measurement of local potential at the sample surface. However, it is certainly not the same as the Hall voltage. Instead, the KPFM signal is dominated by other sources of local surface potential, such as, in our case, that resulting from the applied bias needed to drive the current in the first place. Established literature[30] shows that the absolute Hall voltage can usually be isolated by examining the component in the potential signal that is sensitive to changes in the applied magnetic field: under conditions of constant current, subtracting the potential measurement taken under a magnetic field applied in a nominally positive direction (+B) from that taken under the same magnitude of magnetic field applied in a nominally negative direction (-B) and dividing the resultant by 2 (see schematics Fig 3a and b).

Fig 3c is a lateral-mode PFM map (combined amplitude x phase) of some of the domains within the interelectrode gap, in which a tail-to-tail domain wall is present, the surface trace of which is at ~60º to the applied magnetic field. KPFM images from the same area, when current was driven, under +330mT (Fig 3d) and -330mT (Fig 3e) show domain wall contrast that demonstrably changes upon magnetic field reversal. To quantify field-induced changes and establish Hall voltage values, KPFM potential profiles were taken at 9 sequential line scans in the regions represented by the two blue dashed boxes in the figure panels and, for each scan line, background noise was reduced by applying a peak-preserving Savitsky-Golay filter. Such filtered line profiles, from the boxed region in Fig 3e, are displayed in Fig 3f. These profiles were then spatially realigned, such that the potential troughs associated with the domain wall were coincident, and the mean potential profile across all 9 scans determined (Fig 3g). This process was repeated for the +330mT dataset contained within the boxed region in Fig 3d. When plotted against each other (Fig 3h), the change in measured potential at the domain wall, due to magnetic field reversal, becomes clear. Taking half of the difference between these traces results in a quantification of the Hall voltage. As can be seen in Fig 3i, this Hall voltage is significant (of the order of tens of millivolts) at the domain wall, but modest elsewhere. Indeed, the background signal away from the domain wall is seen to vary between + and – 5mV, which gives some feeling for the uncertainty in the measurement, as the bulk will not simultaneously produce both positive and negative Hall signals. Vector analysis of the current direction, the sense of the change in the magnetic field vector and the resulting positive value in Hall potential shown are consistent with p-type carriers facilitating transport in the tail-to-tail domain walls, as has been seen previously[23].

Similar data, taken under the same magnetic field and current conditions as described above and processed in the same manner, at other tail-to-tail domain walls within the interelectrode gap, gave consistent Hall voltage signs and orders of magnitude values (Fig 4). There was some suspicion that the Hall voltage may have varied depending on the orientation of the domain wall (with respect to the polarisation in the $ErMnO_3$, the applied electric and magnetic fields), but no systematic variations were observed.

The Hall voltage (V_H), measured at the domain walls, can be approximately related to both the carrier mobility (μ) and density (n) as follows (as detailed in previous work[23]):

$$\mu \approx \frac{V_H}{|\mathbf{E}|D|\mathbf{B}|} \qquad \textbf{equation 1}$$

$$n \approx \frac{I_{DW}|\mathbf{B}|}{V_H q \delta_{\text{eff}}} \qquad \textbf{equation 2}$$

where I_{DW} is the current in the domain wall associated with the Hall voltage measurement; $|\mathbf{B}|$ is the magnitude of the magnetic flux density experienced at the wall; q is the carrier charge (assumed to be the magnitude of the electronic charge); δ_{eff} is the effective width of the domain wall; $|\mathbf{E}|$ is the magnitude of the electric field driving the current along the wall and D is the physical depth over which the conducting domain wall channel is active below the sample surface.

Considering the carrier mobility first: for Hall voltages of the order of ~ 30 x 10^{-3} V (typical from data shown in Fig 4), the local electric field, measured explicitly by analysis of the KPFM potential gradients either side of the domain wall (Fig 3g), was found to be of the order of 2 x 10^4 Vm^{-1}, when the applied magnetic field was ~ 0.3T (Vsm^{-2}). The mobility, calculated using equation 1, is hence $\sim(5 \times 10^{-6}/D)$ $m^2V^{-1}s^{-1}$. The value for D had been estimated, in previous work[23], to be of the same order of magnitude as the typical length of the domain wall sections between six-fold junction points, as the microstructure is comparable in all observation orientations [31] and these points might be considered as end-points for the conducting domain walls beneath the crystal surface. Here, we have tried to make more definitive statements, using finite element modelling, about the physical depth of the carrier channel associated with the conducting domain walls. For a uniformly conductive channel, the local current density will simply scale with the local electric field developed when a bias is applied to the electrodes and so

determination of the field distribution, as a function of depth, was the primary focus of the modelling. We used physical dimensions for the $ErMnO_3$ crystal flake (thickness ~200μm) and for the interelectrode gap (~50 μm) that accurately reflected the geometry of the experiment. One surface electrode was set to a positive potential and the other earthed; the lower surface of the crystal was assumed to be earthed (it was not isolated from the metallic platform of the microscope), while sidewall boundary potentials were unfixed. The dielectric permittivity of the domain wall was assumed to be the same as that of bulk $ErMnO_3$ (~300), informed by literature[32], and the carrier density of $10^{13}cm^{-3}$ was inferred from our Hall voltage measurements (see below).

Fig 5a represents a section perpendicular to the crystal surface across the interelectrode gap; the modelled potential map developed is that associated with the above assumed domain wall permittivity and carrier density input information. The electric field component parallel to the crystal surface has been extracted and plotted in Fig 5b and the manner in which this field strength varies with depth is plotted in Fig 5c, at a number of different points across the interelectrode gap. At all points, the field strength is seen to decay monotonically and has a finite value throughout the entire thickness of the $ErMnO_3$. The depth at which the mean electric field occurs, in the distributions shown in Fig 5c, is ~100μm. When this value for D is used in equation 1, the mobility implied is ~500$cm^2V^{-1}s^{-1}$; mobilities in the hundreds of $cm^2V^{-1}s^{-1}$ are comparable to, or higher than, any room temperature bulk or sheet carrier mobilities seen in oxides to date[33–36]. Such high mobility systems have gained recent notoriety for their potential in applications relating to thin film transistors [33–35].

To make inferences about the carrier density within the conducting domain walls (using equation 2), estimates are needed for both the effective wall thickness (δ_{eff}) and the current along each wall (I_{DW}). Previous literature for charged domain walls[37], suggests an effective thickness for the conducting channel of approximately ten nanometres. To estimate the current along each domain wall, we assume that the bulk and domain wall conducting channels between the source and drain electrodes act electrically in parallel.

The resistance ratio between the two microstructural components (R_{bulk}/R_{wall}), which would be equal to the inverse of the ratio of the currents carried, could then be approximated as:

$$\frac{R_{bulk}}{R_{wall}} \approx \frac{\rho_{bulk} L}{A_{bulk}} \cdot \frac{A_{wall}}{\rho_{wall} L} \approx \frac{\rho_{bulk}}{\rho_{wall}} \cdot \frac{\delta_{eff}}{w_{electrode}} \qquad \textbf{equation 3}$$

where ρ_{bulk} and ρ_{wall} are the resistivities of the bulk and wall respectively; A_{bulk} and A_{wall} the cross-sectional areas of the bulk and wall current conduits; L is the length of the interelectrode gap; $w_{electrode}$ the width of each surface electrode. From our conducting atomic force microscopy measurements on these $ErMnO_3$ crystals, the walls appear to be around two orders of magnitude more conductive than the bulk and we assume this is representative of the relative resistivities of the two microstructural components. Previous studies[37] report an I_{wall}/I_{bulk} ratio of approximately 4, at applied voltages considerably smaller than those used during the course of this experiment. The surface electrodes used were ~100μm in width. Equation 3 therefore suggests that $R_{bulk} \sim 1 \times 10^{-2} R_{wall}$ and hence that only around 1nA (from the total of 100nA measured between source and drain) flows through each conducting wall. From equation 2, a carrier density within each wall of ~1 x 10^{13} cm^3 is therefore implied. Comparing these measured carrier densities to estimates of charge density required for screening of polarization discontinuities, at tail-to-tail walls in $ErMnO_3$ (~ 1x10^{20} cm^{-3}), suggests that either the walls are not fully screened, or that the significant majority of screening charges do not take part in conduction[23,38].

The inferred values for carrier mobilities and densities, in the conducting domain walls in the $ErMnO_3$ crystals examined, differ quite significantly from those previously determined in $YbMnO_3$ by Campbell *et al.*[23]. This may obviously be in part because they are different materials systems, but it is certainly also true that the bias fields associated with driving domain wall currents were estimated by Campbell *et al.* as the applied potential difference between source and drain electrodes divided by the interelectrode separation. In the current study, this approach would imply electric fields more than an order or magnitude higher than those actually measured, through examination of the background gradient in the

KPFM potential. Strong potential drops across the electrode-$ErMnO_3$ contact regions can be expected, due to barrier formation, and this has been clearly evidenced by our KPFM study. Direct monitoring of the potential gradient experienced by the $ErMnO_3$ within the interelectrode gap, as opposed to estimates made ignoring the influence of dielectric-electrode potential barriers, is a key reason for the increase in the estimated hole mobilities presented herein. The significant contribution of bulk conduction was also not addressed in prior work and this is the dominant reason for the lower carrier density estimates determined.

To check the validity of data obtained, a separate set of experiments was performed in a similar fashion, on another AFM platform, with associated in-situ variable field magnet system. Figs 6a and 6b show PFM phase maps of a region within the interelectrode gap measured using this new system. On this occasion, a 9 V potential difference was applied to source and drain electrodes to drive a current of approximately 100 nA. A magnetic field reversal technique was once again implemented, using ±400 mT. This second AFM platform allowed KPFM maps with a better signal-to-noise ratio, less drift and reduced image astigmatism. As a result, we were able to align the individual KPFM images taken at positive and negative B-fields and directly determine a Hall potential map (by subtracting the two images and dividing resulting potentials at every point by two). This map is presented in Fig 6c. Importantly, the order of magnitude of the Hall voltages measured, as evidenced in Fig 6d, is similar to those discussed above, under similar measurement regimes. Indeed, extracted mobilities and carrier densities from these data confirm the orders of magnitude estimates associated with the measurements presented in Figs 1 – 4 ($\approx 100 cm^2V^{-1}s^{-1}$ under the same geometric assumptions).

In conclusion, direct and fully quantitative measurements of electric fields and Hall voltages, developed at conducting tail-to-tail charged domain walls in $ErMnO_3$ single crystals, have been made using Kelvin Probe Force Microscopy. This approach overcomes significant hurdles in direct extraction of relevant carrier information at conducting domain walls and could allow further fundamental insight into the conduction mechanisms of known functionally active domain wall systems. It has revealed that the carriers active in the domain walls have strikingly high room temperature mobilities, which we suspect is

associated with the inherent confined conduction geometry and perfect lattice coherence across the domain wall (seen to be important in $LaAlO_3$-$SrTiO_3$ 2DEGS).

Acknowledgements

The authors are extremely grateful to Dennis Meier, Zewu Yan and Edith Bourret for providing the $ErMnO_3$ single crystals examined. The authors acknowledge financial support from the Engineering and Physical Sciences Research Council (contract EP/P02453X/1), the US-Ireland Research and Development Partnership Programme, the Queen's University Belfast Central Research Infrastructure Fund (CRIF) and the Northern Ireland Department for the Economy. We are grateful to Seagate Technology for donation of an atomic force microscope, with in-situ magnetic field capability, that was critical for facilitating the initial research.

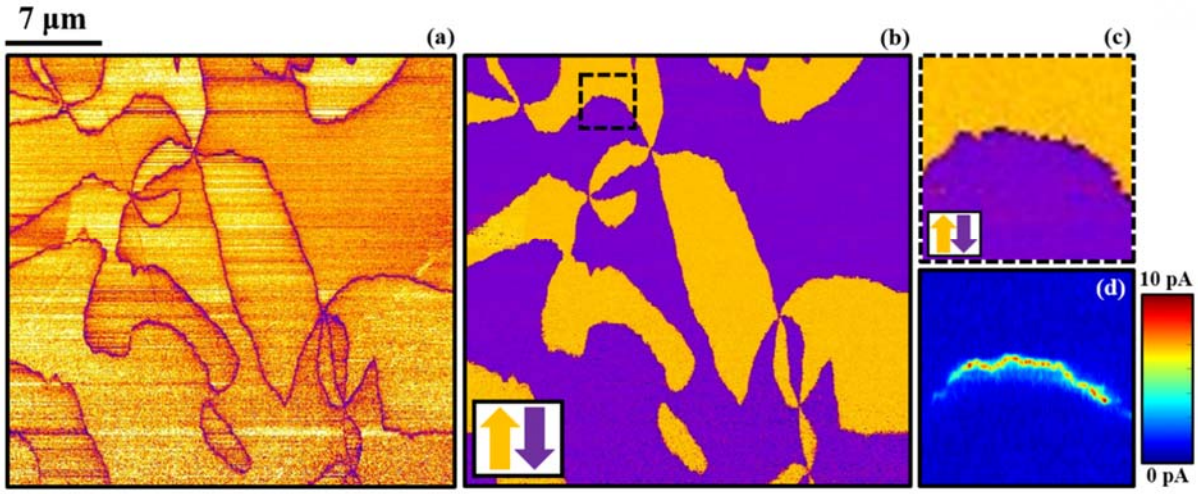

Figure 1. (a) Lateral PFM Amplitude and (b) phase maps display the domain structure in the $ErMnO_3$ single crystals examined. The section in the black dashed box shown in (b) is expanded in (c) and corresponding conductive AFM mapping at 4V applied voltage bias is shown in (d), clearly demonstrating the conductive nature of the tail-to-tail domain walls.

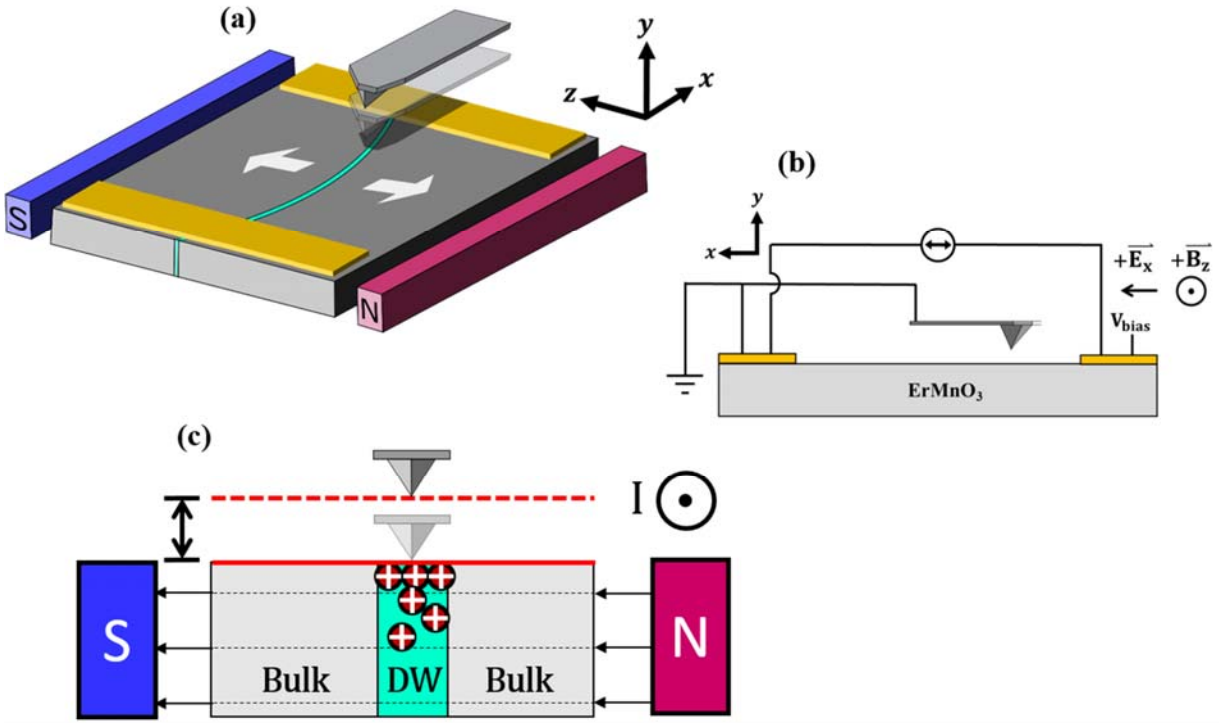

Figure 2. (a) A 3-D schematic of the interleave KPFM method used, with accompanying axis diagram. (b) Side profile diagram of the experimental setup is illustrated. Electrical current is shown to be driven along the x-axis between the Au electrodes. Magnet poles apply a magnetic field along the z-axis**.** (c) Cross-sectional perspective of the bulk crystal and the expected migration of positive charge carriers to the sample top surface. Solid and greyscale cantilever figures demonstrate scanning heights maintained during KPFM and tapping-mode topography scans respectively.

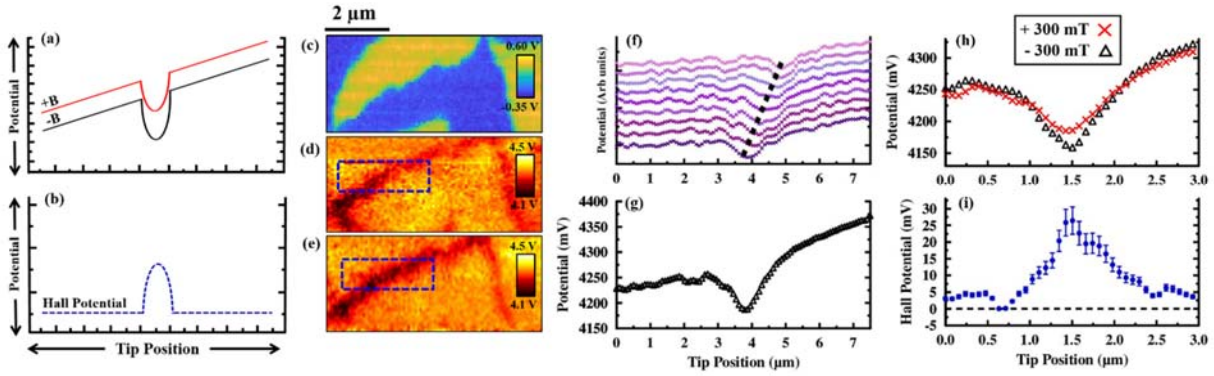

Figure 3. (a,b) Theoretical potential profiles associated with magnetic field reversal Hall effect measurements, applied to p-type carriers active at domain walls in the specific geometry associated with KPFM experiments (the local potential minima occur at the domain walls). The Hall potential is calculated as half of the difference in the electric potential measured when the sense of the applied magnetic field is reversed. (c) Lateral PFM map of the region under test comprising amalgamated phase and amplitude data. Electric potential profiles are extracted from KPFM maps in (d,e): sequential KPFM line scans from within the regions indicated by the blue dashed boxes are shown in (f). Domain wall potential anomalies are aligned and an average of the profiles is taken, as shown in (g). When repeated for a reversed magnetic field (h), half of the difference between averaged line data profiles generates the Hall potential, as displayed in (i).

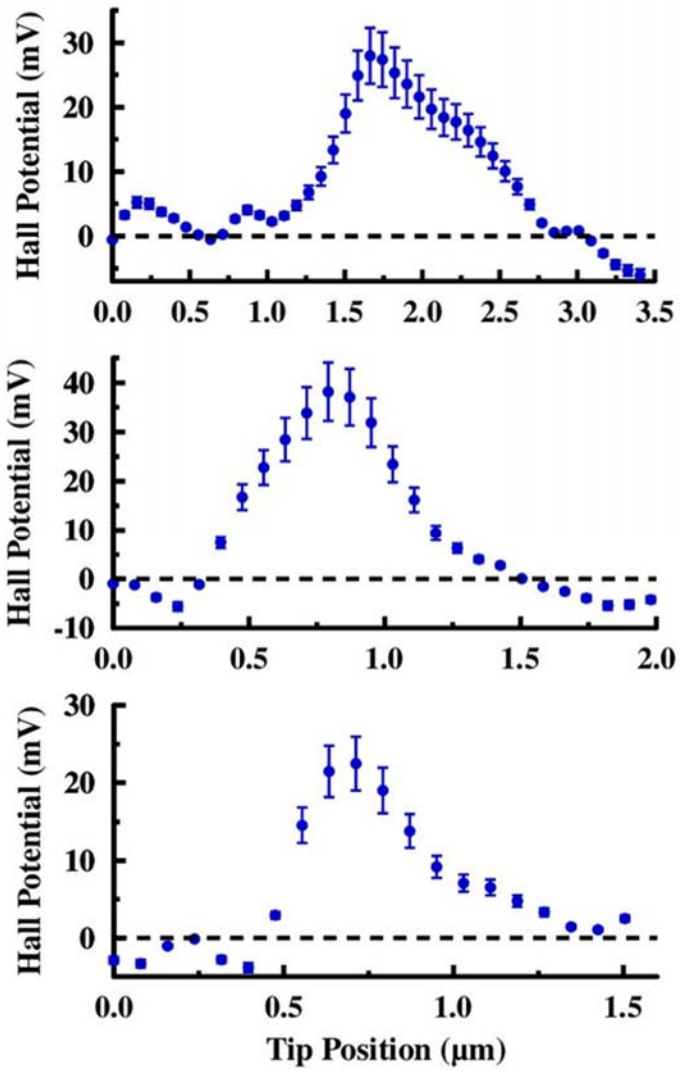

Figure 4. Hall potential profiles measured at 3 tail-to-tail domain walls, in addition to that shown in figure 3, show internal consistency of the data: Hall voltages are of the same sign, consistent with positive charge carrier-mediated conduction, and of similar magnitude.

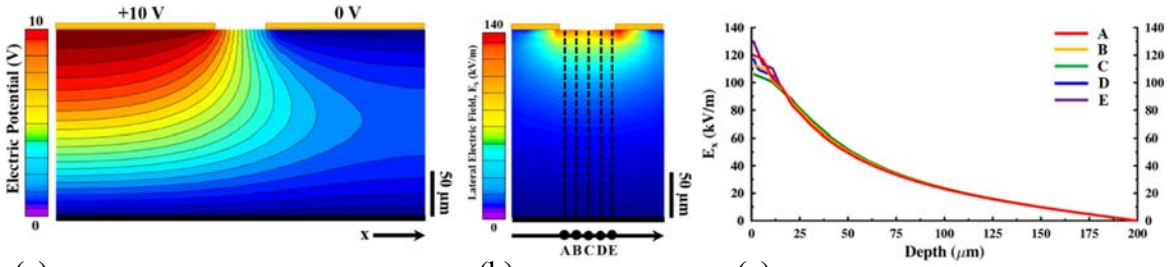

(a) (b) (c)

Fig 5. (a) displays an electric potential map resulting from finite element modelling. A 10 V bias is applied to the gold electrode on the upper left surface of the $ErMnO_3$ crystal sample, with reference to the grounded upper right-hand electrode. The lateral component of the effective electric field extracted from the potential maps, E_x, is displayed in (b). Values of E_x, as a function of depth from the $ErMnO_3$ crystal surface, were taken at several points across the interelectrode gap, plotted in (c). Since finite field penetrates the entire crystal thickness, finite current flow in the domain wall is expected at all depths. Here the mean field depth is at ~75μm.

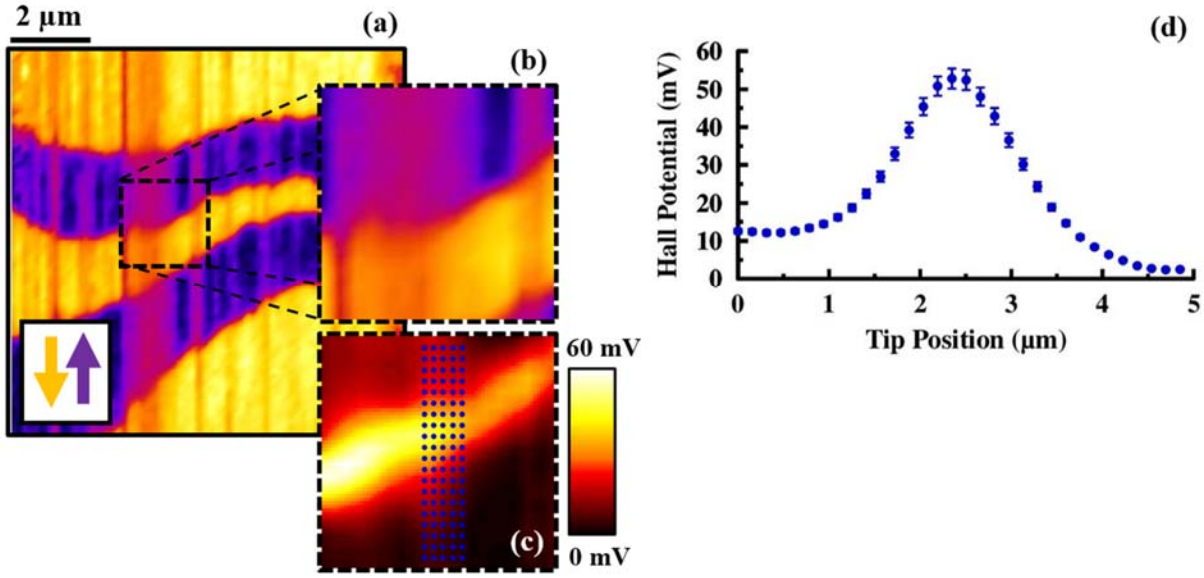

Figure 6. (a) PFM phase map, where yellow and purple arrows indicate the direction of polarisation in ferroelectric domains, taken on an alternative atomic force microscopy (AFM) platform. The dashed section shown in panel (a) is expanded and displayed in (b). (c) The Hall potential map corresponding to the area represented in panel (b). Data from the dotted blue lines in (c) has been averaged to construct a representative Hall potential signal across a tail-to-tail domain wall (d). The sign and magnitude of this signal is consistent with earlier measurements taken on an older AFM platform.

References

1. Zimmermann, A., Bollmann, W. & Schmid, H. Observations of ferroelectric domains in boracites. *Phys. Status Solidi* **3,** 707–720 (1970).
2. Vul, B. M., Guro, G. M. & Ivanchik, I. I. Encountering domains in ferroelectrics. *Ferroelectrics* **6,** 29–31 (1973).
3. Grekov, A. A., Adonin, A. A. & Protsenko, N. P. Encountering domains in sbsi. *Ferroelectrics* **13,** 483–485 (1976).
4. Aird, A. & Salje, E. K. H. Sheet superconductivity in twin walls: experimental evidence of WO3-x. *J. Phys. Condens. Matter* **10,** L377–L380 (1999).
5. Mizuuchi, K., Morikawa, A., Sugita, T. & Yamamoto, K. Efficient second-harmonic generation of 340-nm light in a 1.4-μm periodically poled bulk MgO:LiNbO3. *Japanese J. Appl. Physics, Part 2 Lett.* **42,** 4–6 (2003).
6. Seidel, J. *et al.* Conduction at domain walls in oxide multiferroics. *Nat. Mater.* **8,** 229–234 (2009).
7. Catalan, G., Seidel, J., Ramesh, R. & Scott, J. F. Domain wall nanoelectronics. *Rev. Mod. Phys.* **84,** 119–156 (2012).
8. Guyonnet, J., Gaponenko, I., Gariglio, S. & Paruch, P. Conduction at domain walls in insulating Pb(Zr 0.2Ti 0.8)O 3 thin films. *Adv. Mater.* **23,** 5377–5382 (2011).
9. Sluka, T., Tagantsev, A. K., Bednyakov, P. & Setter, N. Free-electron gas at charged domain walls in insulating $BaTiO_3$. *Nat. Commun.* **4,** 1808 (2013).
10. Schröder, M. *et al.* Nanoscale and macroscopic electrical ac transport along conductive domain walls in lithium niobate single crystals. *Mater. Res. Express* **1,** 35012 (2014).
11. Schröder, M. *et al.* Conducting domain walls in lithium niobate single crystals. *Adv. Funct. Mater.* **22,** 3936–3944 (2012).
12. Meier, D. *et al.* Anisotropic conductance at improper ferroelectric domain walls. *Nat. Mater.* **11,** 284–288 (2012).
13. Oh, Y. S., Luo, X., Huang, F. T., Wang, Y. & Cheong, S. W. Experimental demonstration of hybrid

improper ferroelectricity and the presence of abundant charged walls in (Ca,Sr)3Ti2O7crystals. *Nat. Mater.* **14,** 407–413 (2015).

14. McQuaid, R. G. P., Campbell, M. P., Whatmore, R. W., Kumar, A. & Gregg, J. M. Injection and controlled motion of conducting domain walls in improper ferroelectric Cu-Cl boracite. *Nat. Commun.* **8,** 15105 (2017).
15. Whyte, J. R. & Gregg, J. M. A diode for ferroelectric domain-wall motion. *Nat. Commun.* **6,** 1–5 (2015).
16. Whyte, J. R. *et al.* Ferroelectric Domain Wall Injection. *Adv. Mater.* **26,** 293–298 (2014).
17. McGilly, L. J., Yudin, P., Feigl, L., Tagantsev, A. K. & Setter, N. Controlling domain wall motion in ferroelectric thin films. *Nat. Nanotechnol.* **10,** 145–150 (2015).
18. Parkin, S. S. P., Hayashi, M. & Thomas, L. No Title. **320,** 190–195 (2008).
19. Allwood, D. a. *et al.* Magnetic domain-wall logic. *Science (80-.).* **309,** 1688–1692 (2005).
20. Jiang, J. *et al.* Temporary formation of highly conducting domain walls for non-destructive read-out of ferroelectric domain-wall resistance switching memories. *Nat. Mater.* **17,** 49–55 (2018).
21. Sharma, P. *et al.* Nonvolatile ferroelectric domain wall memory. *Sci. Adv.* **3,** 1–9 (2017).
22. Schaab, J. *et al.* Electrical half-wave rectification at ferroelectric domain walls. 1–28
23. Campbell, M. P. *et al.* Hall effect in charged conducting ferroelectric domain walls. *Nat. Commun.* **7,** 13764 (2016).
24. Cano, A. Hidden order in hexagonal RMnO3 multiferroics. **214107,** 5–9 (2013).
25. Holtz, M. E. *et al.* Topological defects in hexagonal manganites - Inner structure and emergent electrostatics. *Nano Lett.* acs.nanolett.7b01288 (2017). doi:10.1021/acs.nanolett.7b01288
26. Artyukhin, S., Delaney, K. T., Spaldin, N. A. & Mostovoy, M. Landau theory of topological defects in multiferroic hexagonal manganites. *Nat. Mater.* **13,** 42–49 (2013).
27. Fennie, C. J. & Rabe, K. M. Ferroelectric transition in YMnO3 from first principles. *Phys. Rev. B - Condens. Matter Mater. Phys.* **72,** 1–4 (2005).
28. Lilienblum, M. *et al.* Ferroelectricity in the multiferroic hexagonal manganites. *Nat. Phys.* **advance**

on, (2015).

29. Mundy, J. A. *et al.* Functional electronic inversion layers at ferroelectric domain walls. *Nat. Mater.* **16,** 622–627 (2017).
30. Werner, F. Hall measurements on low-mobility thin films. *J. Appl. Phys.* **122,** (2017).
31. Lin, S.-Z. *et al.* Topological defects as relics of emergent continuous symmetry and Higgs condensation of disorder in ferroelectrics. *Nat. Phys.* **10,** 970–977 (2014).
32. Dey, P., Nath, T. K., Goswami, M. L. N. & Kundu, T. K. Room temperature ferroelectric and ferromagnetic properties of multiferroics xLa0.7Sr0.3MnO3-(1-x)ErMnO3(weight percent x=0.1, 0.2) composites. *Appl. Phys. Lett.* **90,** 0–3 (2007).
33. Huang, G., Duan, L., Dong, G., Zhang, D. & Qiu, Y. High-mobility solution-processed tin oxide thin-film transistors with high-κ alumina dielectric working in enhancement mode. *ACS Appl. Mater. Interfaces* **6,** 20786–94 (2014).
34. Fortunato, E. *et al.* High field-effect mobility zinc oxide thin film transistors produced at room temperature. *J. Non. Cryst. Solids* **338–340,** 806–809 (2004).
35. Shih, C. W. & Chin, A. New Material Transistor with Record-High Field-Effect Mobility among Wide-Band-Gap Semiconductors. *ACS Appl. Mater. Interfaces* **8,** 19187–19191 (2016).
36. Kim, H. J. *et al.* High mobility in a stable transparent perovskite oxide. *Appl. Phys. Express* **5,** 3–6 (2012).
37. Schaab, J. *et al.* Optimization of Electronic Domain-Wall Properties by Aliovalent Cation Substitution. *Adv. Electron. Mater.* **2,** (2016).
38. Stolichnov, I. *et al.* Persistent conductive footprints of 109° domain walls in bismuth ferrite films. *Appl. Phys. Lett.* **104,** 1–5 (2014).